Biosensors and Bioelectronics 144 (2019) 111663

Contents lists available at ScienceDirect

Biosensors and Bioelectronics

journal homepage: www.elsevier.com/locate/bios

A versatile ratiometric electrochemical sensing platform based on N-Mo_2C for detection of m-nitrophenol

Hailong Ren[a], Jingjing Wang[b], Huanhuan Feng[c,*], Yingchun Li[b,d], Bang-Ce Ye[a,e,**]

[a] Key Laboratory for Green Processing of Chemical Engineering of Xinjiang Bingtuan, School of Chemistry and Chemical Engineering, Shihezi University, Shihezi, 832000, China
[b] Key Laboratory of Xinjiang Phytomedicine Resources for Ministry of Education, School of Pharmacy, Shihezi University, Shihezi, 832000, China
[c] School of Materials Science and Engineering, Harbin Institute of Technology (Shenzhen), Shenzhen, 518055, China
[d] School of Science, Harbin Institute of Technology, Shenzhen, 518055, China
[e] State Key Laboratory of Bioreactor Engineering, East China University of Science and Technology, Shanghai, 200237, China

ARTICLE INFO

Keywords:
N-Mo_2C
Methylene blue
Electrochemical detection
Ratiometric
Square wave voltammetry
m-NP

ABSTRACT

M-nitrophenol (m-NP) is a high priority environmental pollutant and poses a series of threats on human health. Accurate and rapid detection of m-NP in practical samples is very important as this is the key prerequisite for its effective monitoring. Eelectrochemical sensor, though long serving as highly sensitive and fast analytical tool, suffers from the bottleneck problems like low specificity, poor reproducibility, susceptibility to internal and external disturbances, etc. Herein, we developed a ratiometric electrochemical sensor (R-ECS) for m-NP detection, in which nitrogen-doped Mo_2C (N-Mo_2C) was deployed as the sensing agent and methylene blue (MB) as the internal reference. Full characterization of N-Mo_2C was carried out in the aspects of morphology, composition, chemical bonds and electrochemical behavior, and the sensing performance of the easy-to-operate R-ECS was evaluated. Complete separation of the oxidation peaks of m-NP and MB was achieved using the MB/N-Mo_2C composite modified electrode and their ratiometric signals were adopted for quantification of m-NP. The linear relation between the electrical signal and the concentration of m-NP is in the range of 1–1500 μM, with the detection limit of 0.256 μM (S/N = 3). The sensor was applied to measure m-NP in real samples from tap water and river. Experimental results demonstrate that it exhibits decent repeatability, reproducibility, stability and selectivity, which proves its great practical potential as an analytical detector.

1. Introduction

Nitrophenol is widely used in producing pesticides, dyes, pharmaceuticals, textiles, paper and explosive materials. In 1976, the United States Environmental Protection Agency classified nitrophenol as a hazardous substance and a priority toxic pollutant (Asadpour-Zeynali and Najafi-Marandi, 2011). Due to its toxicity, excessive inhalation of nitrophenol in humans and animals can cause high fever, methemoglobin and kidney damage (Honeychurch and Hart, 2010). Irrigation of plant crops with water containing above 0.7 mM of m-nitrophenol (m-NP) will lead to decrease in production (Silvester et al., 2006). At present, the methods of monitoring nitrophenol include flow injection analysis (Belloli et al., 1999), spectrophotometry (Gu et al., 2011), capillary electrophoresis (Guo et al., 2004), high performance liquid chromatography (Niazi and Yazdanipour, 2007), spectroscopy (Perry et al., 2010) and electroanalysis (Chu et al., 2011). Electrochemical(Li et al., 2018; Li et al., 2016; Zhang et al., 2018c) tactics have attracted more and more attention owing to their high speed, simple operation and low cost. However, traditional electrochemical sensors suffer from low selectivity, and poor stability and robustness. Thus, search for appropriate catalysts to facilitate electrochemical reaction of target analyte at certain potential is of great significance.

Traditional electrochemical sensors only have single electrical signal which is susceptible to the inevitable variations in sensor preparation, detection environment, operation procedure, etc., resulting in poor accuracy and stability (Liu et al., 2019; Wang et al., 2016; Yi et al., 2015). In recent years, by introducing an electroactive substance as internal reference (IR) and employing the ratio response between analyte and IR substance for quantification, it is expectable to overcome these defects, thereby improving repeatability, stability and robustness of the sensor (Hanjun et al., 2015). Currently, common ratio electrochemical sensors have two working modes. The first one is to

* Corresponding author.
** Corresponding author. School of Science, Harbin Institute of Technology, Shenzhen, 518055, China.
E-mail addresses: fenghuanhuan@hit.edu.cn (H. Feng), liyingchun@hit.edu.cn (Y. Li), bcye@ecust.edu.cn (B.-C. Ye).

https://doi.org/10.1016/j.bios.2019.111663
Received 27 June 2019; Received in revised form 23 August 2019; Accepted 28 August 2019
Available online 03 September 2019
0956-5663/

immobilize IR molecules at an electrode (Hanjun et al., 2015; Zhang et al., 2018b) and the second mode is to add reference molecules to electrolyte solution (Yu et al., 2017; Zhang et al., 2019). In comparison, the first mode avoids the error caused by adding IR molecules repeatedly in electrolyte solution; however, the difficulty in modification of IR onto electrode still exists. At present, IR molecules can be fixed on electrode surface by electrochemical polymerization (Li and Kan, 2018), covalent bond binding (Yan et al., 2014), formation of complexes with assistance of cage-shaped substances (Xia et al., 2015), etc., but these methods have the disadvantages of harsh conditions and complicated operation process. For example, electrochemical polymerization requires specific conditions (electrolyte solution, polymerization potential, pH value, etc.) to allow for polymerization reaction. Covalent binding is stable but difficult to apply on a large scale due to the requirement of specialized instruments and operation. Although interlocking of IR molecules by supramolecules (e.g. cyclodextrin and calixarene) is easy, fixation of supramolecules adds extra work. Herein, we adopted a facile tactic by first combining IR molecules with nano-materials using simple ultrasonic treatment and then drop-coating of the composite on electrode. Selection of IR molecules and derivatization of nano-materials were carried out in order to ensure their firm combination.

In previous reports, various molybdenum-based materials have been developed (e.g. molybdenum disulfide (Berit et al., 2005; Kong et al., 2016), molybdenum phosphide (Mcenaney et al., 2014), molybdenum nitride (Zhu et al., 2017) and molybdenum carbide (Feng et al., 2014)) and attracted wide attention due to their low cost and high chemical stability. In particular, it was found that the electronic structure of molybdenum carbide (Mo_2C) is similar to that of Pt–group metals, which is extremely favorable to act as high-efficient catalyst in building electrochemical sensor. Additionally, carbon matrix treated with nitrogen doping has been reported to show n-type behavior (Chen et al., 2018), which endows metallic property to the material, increases the type and number of active sites, and benefits electron transfer rate. Therefore, N-Mo_2C owns the promising potential as an ideal sensing agent to improve the performance of electrochemical sensor.

Here, we developed a novel electrochemical sensor based on nitrogen-doped Mo_2C (N-Mo_2C) nanoparticles. It was found that introduction of N-Mo_2C nanoparticles increased electrical conductivity, enlarged specific surface area, provided abundant surface groups, and benefited electrochemical reaction of m-NP as well. Further modification of the N-Mo_2C based sensor with reference molecules (methylene blue) allows for ratiometric quantification of the target molecules. The sensor has been successfully applied to detect m-NP in tap water and river water samples.

2. Experimental section

2.1. Reagents and instruments

M-nitrophenol (m-NP), ammonium molybdate tetrahydrate ($(NH_4)_6Mo_7O_{24}{\cdot}4H_2O$), urea, dopamine hydrochloride (DA-HCl) and methylene blue (MB) were bought from Adamas Reagent Co. Ltd. (Shanghai, China; www.tansoole.com). Other chemical reagents, such as HCl, NaOH, $K_3[Fe(CN)_6]$, $K_4[Fe(CN)_6]$, KNO_3, KCl, KH_2PO_4, K_2HPO_4 and ethanol were obtained from Titan Scientific Co. Ltd. (Shanghai, China; www.tansoole.com). All solutions were prepared via doubly distilled water (DDW).

All electrochemical experiments, including cyclic voltammetry (CV), electrochemical impedance spectroscopy (EIS) and square wave voltammetry (SWV), were carried out with a CHI760E electrochemical workstation (Chenhua Instruments Co, Shanghai, China; www.chinstr.com). A classical three-electrode system consists of a saturated calomel electrode (SCE), a platinum wire (0.5 mm in diameter) and a bare or modified glassy carbon electrode (GCE, 4 mm diameter) as the reference, auxiliary and working electrode, respectively. The morphology of materials was observed with scanning electron microscopy (SEM, Hitachi S-4800, Japan) and transmission electron microscope (TEM, TF20, Jeol 2100, Japan). The specific surface area of materials was conducted with a Brunauer-Emmett-Teller (BET, Quantachrome NOVA 1000) experiment. Fourier transform infrared (FTIR) spectroscopy was used to analyze phase structure on Nicolet iS50 spectrometer (Thermofisher, America). X-ray photoelectron spectroscopy (XPS) was operated using an Al 18 Kα X-ray source (Escalab 250, Thermo Fisher Scientific, USA). X-ray powder diffraction (XRD) was applied for structure characterization on a Bruker D8 advance X-ray diffractometer (Cu-Kα, λ = 1.5418 Å, Bruker XFlash-SDD-5010, Germany) from 10° to 90°. The UV–Visible spectrophotometer (UV) from China. (UV-5100, Shanghai, China).

2.2. Synthesis of N-Mo_2C

Firstly, 180 mg $(NH_4)_6Mo_7O_{24}{\cdot}4H_2O$ and 100 mg urea were dissolved in 60 mL DDW, which was named as solution (I); 250 mg of Dopamine hydrochloride was dissolved in 120 mL absolute ethanol and marked as solution (II). Then, solution (II) was added dropwise into solution (I) under rapid stirring at room temperature, and pH of the mixture was adjusted by 25–28% ammonium hydroxide. The above solution was transferred into a stainless steel autoclave and heated at 180°C for 12 h. After cooling to room temperature, nitrogen doped Mo-polydopamine (N-MPD) precursor was collected by centrifugation at 5000 rpm for 10 min and washed with absolute ethanol, followed by drying at 60°C. In the end, the precursor was annealed at certain temperature in Ar with a heating rate of 5 °C min^{-1} to obtain N-Mo_2C. The pH of N-MPD, the annealing temperature and time in preparing N-Mo_2C were optimized in order to obtain the best catalytic performance. Detailed experiments and result were displayed in the Supplementary-materials file (Fig. S1).

2.3. Preparation of MB/N-Mo_2C nanocomposites

The MB/N-Mo_2C nanocomposites were prepared as follows. 2 mg N-Mo_2C was dispersed into 1 mL MB solution (30 mM). The suspension was sonicated for 5 h at room temperature, and then centrifugated at 13,000 rpm for 5 min. After washing with DDW and drying in a vacuum oven at 60°C for 12 h, the formed MB/N-Mo_2C nanocomposites were re-dispersed in 1 mL DDW for subsequent experiments.

2.4. Fabrication of MB/N-Mo_2C/GCE

Bare GCE was polished repeatedly to a mirror with 0.3 μm and 0.05 μm alumina power slurries, and then thoroughly cleaned with DDW and ethanol, and dried at room temperature. After that, 4 μL of the suspension was drop-coated onto surface of GCE and dried under an infrared light. The preparation scheme of MB/N-Mo_2C/GCE is illustrated in Fig. 1.

2.5. Electrochemical measurement

CV, EIS and SWV were used to characterize electrochemical properties of differently modified electrodes. CV experiment was carried out in probe solution containing 5 mM $[Fe(CN)_6]^{3-/4-}$ and 0.1 M KCl with potential range from −0.2 V to 0.6 V at a scan rate of 100 mV s^{-1}. EIS performance was studied in probe solution in the frequency range from 0.01 Hz to 100 kHz. SWV measurement was operated in different concentrations of m-NP in a potential range of −0.5–0.1 V.

3. Results and discussion

3.1. Morphology and structural study of N-MPD and N-Mo_2C

The morphologies of N-MPD and N-Mo_2C were observed with SEM

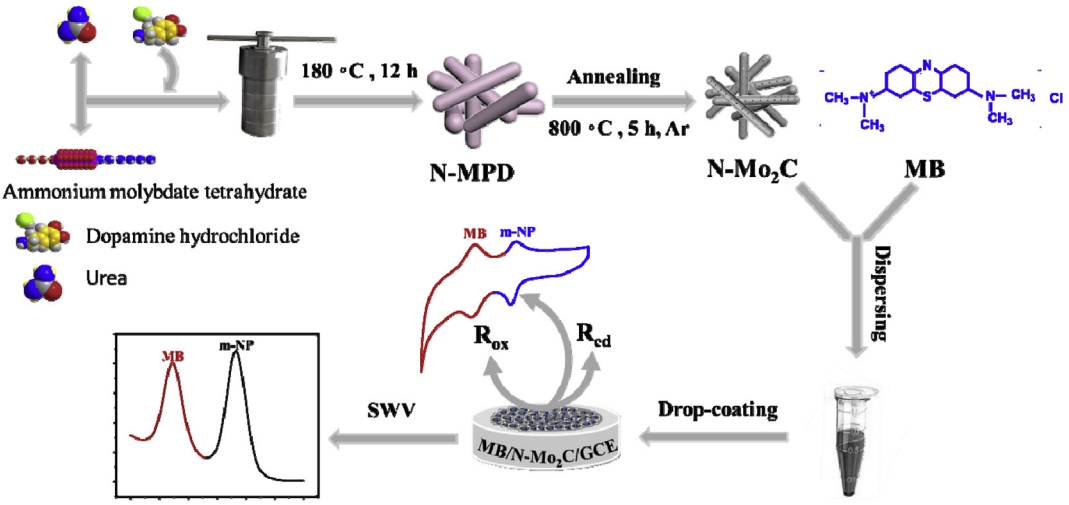

Fig. 1. The schematic representation of MB/N-Mo_2C/GCE preparation.

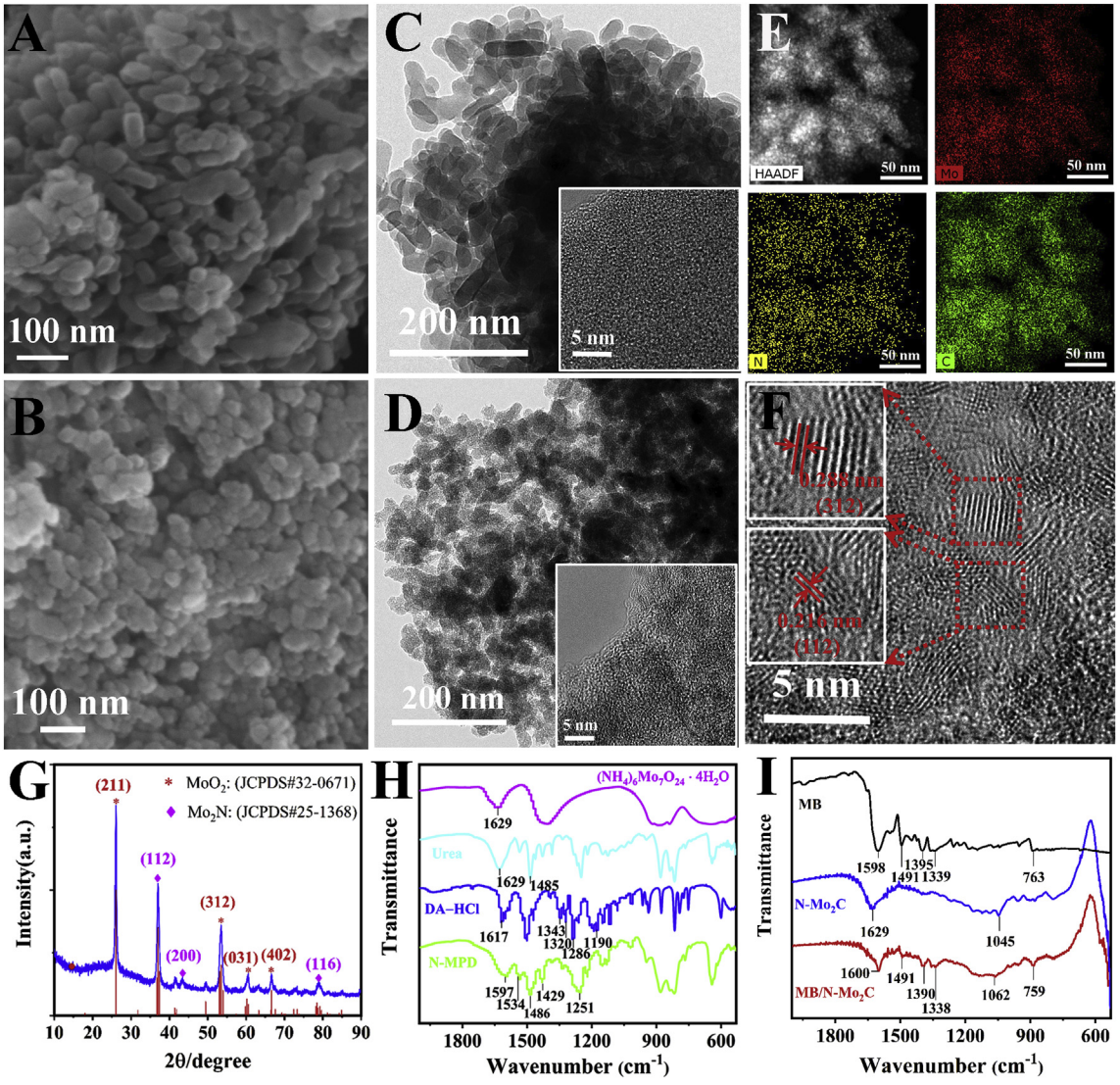

Fig. 2. SEM of N-MPD (A) and N-Mo_2C (B). TEM of N-MPD (C) and N-Mo_2C (D). High-angle annular dark field (HAADF) and EDS mapping image of N-Mo_2C (E). HRTEM images of N-Mo_2C (F). XRD patterns of N-Mo_2C (G). FTIR spectra of (H) $(NH_4)_6Mo_7O_{24}$•$4H_2O$, CH_4N_2O, DA-HCl and N-MPD, (I) MB, N-Mo_2C and MB/N-Mo_2C. (Inset: Higher resolution image).

and TEM (Fig. 2). As shown in Fig. 2A and B, N-MPD and N-Mo_2C are small rod-shaped nanoparticles with size diameter of about 20–50 nm. The particle size of N-Mo_2C is smaller compared with its precursor N-MPD, which could arise from pyrolysis of some organic ligands and collapse of some organic skeletons after annealing. TEM images of N-MPD and N-Mo_2C confirmed the formation of porous structure as shown in Fig. 2C and D. Brunauer-Emmett-Teller (BET) experiment was performed to assess the specific surface area of N-MPD and N-Mo_2C. The results shown that the specific surface area of N-MPD was 39.94 $m^2 g^{-1}$ and that of was N-Mo_2C 87.26 $m^2 g^{-1}$ (Figs. S2A and S2B). Besides, the average pore size of N-MPD and N-Mo_2C were 42.57 nm and 28.74 nm, respectively. In Fig. 2E, the high-angle annular dark field (HAADF) and energy dispersive X-ray spectroscopy (EDS) element mapping images of N-Mo_2C further demonstrate the porous architecture and the uniform distribution of Mo, N and C elements in materials. The high resolution transmission electron microscopy (HRTEM) image (Fig. 2F) reveal the lattice plane distance of about 0.288 and 0.216 nm, which are in good agreement with the (312) and (112) planes of MoO_2 and Mo_2N, respectively. All the above features clearly indicate the successful synthesis of N-Mo_2C.

The structure and the composition of N-Mo_2C were characterized by Xray diffraction (XRD) (Fig. 2G). The obvious diffraction peaks of N-Mo_2C appeared at 26.15°, 53.62°, 60.54° and 66.67° corresponding to the (211) (312) (031) and (402) planes of MoO_2 (JCPDS # 32–0671), respectively. The peaks at 37.07, 43.09 and 78.34 corresponding to (112), (200) and (116) planes were conformed to Mo_2N (JCPDS # 25–1368). It shows that there are some interactions between Mo_2N and MoO_2. In addition, a peak of amorphous carbon around 25.6° can also be observed. The results further verify that N-Mo_2C was successfully synthesized.

The bonding characterization of $(NH_4)_6Mo_7O_{24}{\cdot}4H_2O$, CH_4N_2O, DA − HCl, N-MPD, and N-Mo_2C by Fourier transform infrared spectroscopy (FTIR) is shown in Fig. 2H. The absorption band of $(NH_4)_6Mo_7O_{24}{\cdot}4H_2O$ at 1629 cm^{-1} is ascribed to the bending vibrations of N–H. The peak centered at 1629 cm^{-1} and 1485 cm^{-1} are assigned to stretching vibration of carbonyl, N–H and C–N in CH_4N_2O. The characteristic peak at 1617 cm^{-1} belongs to bending vibration of N–H in DA − HCl. The absorption bands at 1343 cm^{-1}, 1320 cm^{-1}, 1286 cm^{-1} and 1190 cm^{-1} are distributed to flexural vibration of O–H and stretching vibration of C–O on benzene ring. After polymerization, some distinct peaks appear at 1597, 1534, 1486, 1429 and 1251 cm^{-1}. These peaks are due to bending vibration of C-C═N, suggesting the formation of indole structure. In Fig. 2I, the bands of MB at 1491 cm^{-1} and 1395 cm^{-1} are ascribed to stretching vibration of $–CH_3$. The bands at 1598 cm^{-1}, 1339 cm^{-1} and 763 cm^{-1} are attributed to stretching vibration of benzene ring skeleton, and bending vibration of C-N and C-S, respectively. On the other hand, the sharp peaks of N-Mo_2C observed in 1595 cm^{-1} and 1384 cm^{-1} arise from C═C stretching vibration of aromatic rings and C-N-H bending vibration of indole structure. In comparison, the IR spectrum of MB/N-Mo_2C contains the characteristic absorption peaks of MB (1491 cm^{-1}, 1390 cm^{-1}, 1338 cm^{-1} and 759 cm^{-1}) and N-Mo_2C (1600 cm^{-1} and 1062 cm^{-1}).

Surface chemical properties and elemental composition of N-Mo_2C were further investigated by X-ray electron spectroscopy (XPS) (Fig. S3). The XPS wide-scan spectrum (Fig. S3A) shows different peaks located at around 231.08 (Mo 3d), 283.08 (C 1s), 397.08 (N 1s) and 529.08 eV (O 1s), which illustrate N-Mo_2C was successfully synthesized. Fig. S3B shows that high-resolution C 1s XPS spectrum can be attributed to Mo-C/C–C (284.7 eV), N–C/N═C (285.9 eV) and C═O (289.3 eV) (Pu et al., 2016). Meanwhile, the high-resolution XPS Mo 3d spectrum (Fig. S3C) can be ascribed to Mo^{2+} (228.87 eV, 229.07 eV), Mo^{4+} (232.77 eV) and Mo^{6+} (236.17 eV). Mo^{2+} is derived from Mo_2C and Mo_2N (Liu et al., 2013). For Mo^{4+} and Mo^{6+}, they come from molybdenum oxides (MoO_2 and MoO_3). The N 1s XPS spectrum (Fig. S3D) exhibits three sub peaks, in which the peaks located at 394 eV, 399.5 eV and 401.5 eV can be assigned to pyridinic N, pyrrolic N and quaternary N, respectively (Chen et al., 2016; Du et al., 2016). The presence of the 394.60 eV peak indicates the successful obtained of N-Mo_2C.

3.2. Electrochemical characteristics of N-MPD and N-Mo_2C

The electrochemical properties of different materials modified GCE were characterized by CV and EIS in probe solution. As shown in Fig. S4A, after N-MPD modification, redox peak currents of N-MPD/GCE decreased, which is ascribed to the poor conductivity of N-MPD that hinders the transport of electrons. In contrast, the peak current value of N-Mo_2C/GCE increased apparently compared with bare GCE. This can be attributed to the good conductivity and the porous architecture of N-Mo_2C, thereby promoting the electron transfer rate. Subsequently, after decoration of MB on N-Mo_2C, the redox peaks remain almost constant, implying that MB molecules have no apparent effect on electrochemical property of N-Mo_2C. Meanwhile, electron-transfer resistance (R_{et}) was calculated through the diameter of semicircle of EIS curve (Fig. S4B), and the resistance of bare GCE, N-MPD/GCE, N-Mo_2C/GCE and MB/N-Mo_2C/GCE are fitted as 89.2 Ω, 542.7 Ω, 7.3 Ω and 7.8 Ω, respectively, which is in good consistency of CV results.

The electrocatalytic properties of different electrodes was investigated via SWV in 0.1 M PB (pH 7.0) containing 100 μM m-NP (Fig. S4C). It is obvious that the peak current of m-NP is minimal at N-MPD/GCE, which is attributed to the poor conductivity of N-MPD hindering the transfer of electrons. In comparison, the peak current of m-NP at N-Mo_2C/GCE and MB/N-Mo_2C/GCE increases by about 4 times and 3 times relative to the bare GCE. These enhanced peak currents at MB/N-Mo_2C/GCE indicate that the MB/N-Mo_2C composites play good catalytic effect on electro-oxidation of m-NP.

3.3. Influence of pH and scan rate

The effect of pH on electrocatalytic performance at MB/N-Mo_2C/GCE was studied by SWV in 0.1 M PB containing 0.1 mM m-NP (Fig. S5A). As shown in Fig. S5B, MB and m-NP display the same tendency that their peak currents first increased and then decreased with the increase of pH value from 6.0 to 8.5, and the largest responses of both compounds were obtained at pH 7.0. To get more insight about the electrooxidation mechanism of m-NP and MB, the dependence of peak potential on pH was studied. In Fig. S5C, with the rise in pH, peak potentials of MB and m-NP were negatively shifted, suggesting that protons participated in the oxidation reaction (Wang et al. 2012, 2017). The relationships between pH and peak potentials are $E_{m\text{-}NP}$ (V) = 0.0314–0.0543 pH (R^2 = 0.9991) and $E_{m\text{-}NP}$ (V) = 0.2713–0.0572 pH (R^2 = 0.9969). The slopes of both equations are close to −0.059 V pH^{-1}, the slope of the Nernst equation of $E = E^0 - (0.059\ m/n)$ pH (Jing et al., 2014), implying that the number of protons (m) and electrons (n) in charge transfer is substantially equal. Since pH 7.0 gave rise to the highest response, it was selected for the subsequent experiments.

In order to better study the reaction mechanism of m-NP at MB/N-Mo_2C/GCE, the effect of scan rate on its electrochemical reaction was explored by CV. As can be seen in Fig. S5D, the redox peak current of m-NP increased and peak potential shifted positively with raising scan rate from 10 to 200 mV s^{-1}. The corresponding relation is summarized in Fig. S5E, where a linear relationship between redox peak current of m-NP and the square root of scan rate was obtained. The same relation was also found in the case of MB (Fig. S5F).The result suggests that the electrochemical reaction of m-NP at MB/N-Mo_2C/GCE is a diffusion controlled process.

CV scanning of MB/N-Mo_2C/GCE in 0.1 mM m-NP (pH 7.0) at a scan rate of 100 mV s^{-1} was recorded and shown in Fig. S6A. The reduction peak (R) at −0.65 V comes from the reduction of nitro group to hydroxyl amino group through four electron transfer(Luo et al., 2008; Pearson, 1948; Shi and Diao, 2011). The electrochemical reactions of m-NP are reversible, and the number of electrons transferred during the

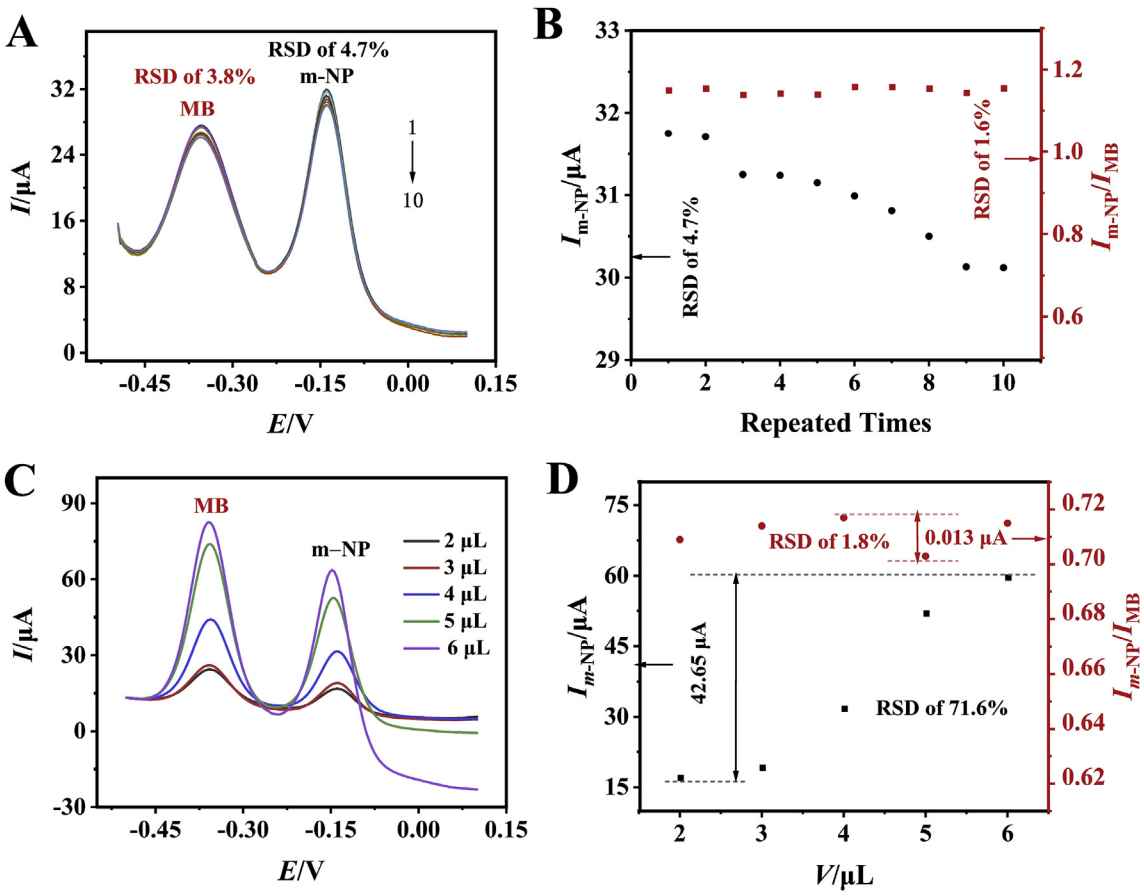

Fig. 3. SWV plots of MB/N-Mo_2C/GCE in PB (pH 7.0) with 100 μM m-NP for continuous measurements of 10 times (A). Each measurement was followed with fully water rinsing treatment of the electrode. Plots of non-ratiometric and ratiometric electrochemical responses versus repeating measurement times (B). SWV plots of different amounts of MB/N-Mo_2C/GCE in 0.1 mM PB (pH 7.0) containing 50 μM m-NP (C). Plots of non-ratiometric and ratiometric electrochemical response for detecting m-NP by different amounts of MB/N-Mo_2C modified GCE (D).

process was calculated by the following equation (Vondrák, 1983; Zhang et al., 2018a):

$$|Ep - Ep/2| = 2.2RT/nF = 0.0565/n$$

where E_p is the peak potential and $E_{P/2}$ is the potential at half of the peak current. R is gas constant (8.314 J mol^{-1} K^{-1}) and n refers to number of electrons participating in the redox reaction (Table S1). T is Kelvin temperature (298.15 K) and F is Faraday constant (96,498 C mol^{-1}). Two electrons and two protons are involved in the redox process and the reaction equation of m-NP is given in Fig. S6B.

3.4. Ratiometric electrochemical detection of m-NP with MB/N-Mo_2C/GCE

In order to prove the robustness of the R-ECS, the following experiments were conducted. After each determination, MB/N-Mo_2C/GCE was taken out and thoroughly rinsed with double distilled water. As illustrated in Fig. 3A, the peak currents of MB and m-NP reduced gradually after each washing treatment, which could be caused by loss of MB/N-Mo_2C from electrode surface due to the cleaning process. The relative standard deviation (RSD) of $I_{m\text{-}NP}$ in 10-times measurements was calculated to be 4.7%, while RSD of $I_{m\text{-}NP}/I_{MB}$ was reduced to 1.6% (Fig. 3B). The results suggest the much enhanced robustness and reliability afforded by R-ECS compared to its non-ratiometric counterpart, which is advantageous to multiple usage.

To further investigate the extraordinary merits of R-ECS as a detection tool, we intentionally changed the amount of MB/N-Mo_2C dispensed onto GCE surface. As shown in Fig. 3C, the peak currents of MB and m-NP changed significantly with alteration of the amount of MB/N-Mo_2C. However, it can be seen from Fig. 3D that the RSD of $I_{m\text{-}NP}$ was calculated to be 71.6%, while the ratiometric signals of $I_{m\text{-}NP}/I_{MB}$ remained almost constant with small RSD of 1.8% (n = 5). Therefore, it can be concluded that the introduction of IR substance can effectively calibrate detecting results and overcome the impacts from environment and individuals, which successfully enhances the robustness of sensors.

Under the optimal conditions, the performance of the as-designed MB/N-Mo_2C/GCE toward ratiometric detection of m-NP was explored via SWV. As shown in Fig. 4A and B, with the increase of m-NP concentration from 1 to 1500 μM, the oxidation peak current of m-NP increased while the peak current of MB remained unchanged, suggesting that MB molecules are firmly adsorbed on N-Mo_2C and the oxidation reaction of MB molecules is well reversible. Fig. 4C exhibits the good logarithmic dependence of $I_{m\text{-}NP}$ on m-NP concentration. The non-ratiometric linear regression equation is $\lg(I_{m\text{-}NP}) = 0.4119 + 0.4314 \lg C$ ($R^2 = 0.9958$), with the limit of detection (LOD) of 0.256 μM (S/N = 3). A ratiometric linear relationship between logarithm of $I_{m\text{-}NP}/I_{MB}$ and logarithm of m-NP concentration was shown in Fig. 4D, and the linear equation is expressed as $\lg(I_{m\text{-}NP}/I_{MB}) = -0.9029 + 0.4444 \lg C$ ($R^2 = 0.9983$). Compared with non-ratiometric sensor, the correlation coefficient of ratiometric sensor is better. The results show that the ratiometric electrochemical strategy equipped with a built-in correction can further improve accuracy and sensitivity in electrochemical sensing. A comparison of some main performance between our sensor and other previously reported electrochemical methods is summarized in Table 1.

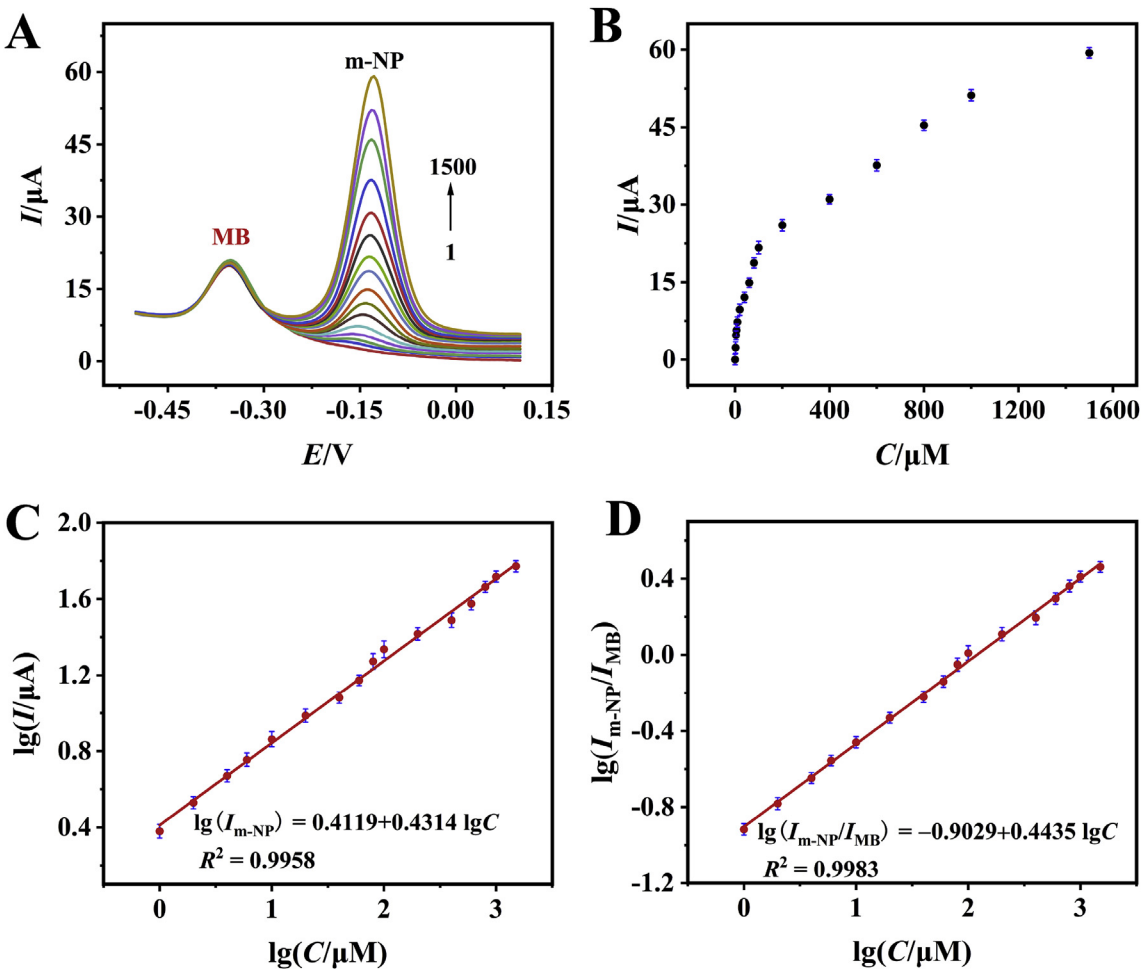

Fig. 4. (A) SWV responses at MB/N-Mo_2C/GCE in different concentrations of m-NP (from 1 to 1500 μM) in 0.1 M PB (pH 7.0); (B) the relation between peak current and concentration of m-NP; the calibration curves correlating the logarithm of (C) $I_{m\text{-}NP}$ and (D) $I_{m\text{-}NP}/I_{MB}$ with the logarithm of m-NP concentration.

Table 1
Comparison of MB/N-Mo_2C/GCE with other reported electrochemical sensors in m-NP detection.

Electrode	Method	Linear range (μM)	LOD (μM)	Ref.
CD-RGO[a]/GCE	DPV	7.0–43	0.7	Liu et al. (2012)
OMCs[b]/GCE	DPV	1.0–100	0.06	Zhang et al. (2013)
Poly(p-ABSA)[c]/GE	SDV	3.0–700	0.5	Yao et al. (2015)
Polyfurfural film/GCE	DPV	0.75–100	0.05	Wei et al. (2015)
CD-SBA[d]/CPE	DPD	2–16	0.05	Xu et al. (2011)
MB/N-Mo_2C/GCE	SWV	1.0–1500	0.256	This work

[a] CD-RGO: Cyclodextrin-Reduced graphene oxide.
[b] OMCs: ordered mesoporous carbons.
[c] Poly(p-ABSA)/GE: Poly(p-aminobenzene sulfonic acid)-modified graphite electrode.
[d] CD-SBA: β-cyclodextrin functionalized SBA-15.

3.5. Selectivity, repeatability, reproducibility and stability of MB/N-Mo_2C/GCE

Selectivity study at MB/N-Mo_2C/GCE was investigated by determination of m-NP (50 μM) and mixtures of m-NP and potential interferents that may be present in water. The tested interferents include several ions (Na^+, K^+, Ca^{2+}, Cu^{2+}, Mg^{2+}, Zn^{2+}, Cl^-, NO_3^-, SO_4^{2-}) and molecules (*o*-nitrophenol, *p*-nitrophenol, phenol, ascorbic acid, bisphenol A, humic acid, glucose), and their concentration is ten times higher than that of m-NP. In Fig. 5A, compared with m-NP alone, the responses from the mixtures have no obvious difference and the relative signal change is less than 5%. These results confirmed good selectivity of the proposed sensor for detecting m-NP in real samples.

Stability of the ratio sensor in immobilizing the inner-reference molecule-MB, was studied by 20-times continuous SWV scanning of the electrode in 0.1 M PB (pH 7.0). As exhibited in Fig. 5B, the peak current of MB was almost unchanged with RSD of 1.95% during the 20-times scanning, indicating that MB was well-combined with N-Mo_2C and generated stable reference signals.

In the case of reproducibility evaluation, six MB/N-MO_2C/GCE were prepared following the same process and adopted to measure 50 μM m-NP. RSD of the tested current signals is 3.57%, implying that the sensor fabrication procedure and the electrochemical method are highly reproducible. In order to examine the long-term stability, MB/N-Mo_2C/GCE was stored at 4 °C when not in use. After 14 days, the oxidation peak currents of MB and m-NP were 96.9% and 94.5% of the initial values, indicating that MB/N-Mo_2C/GCE features great stability for practical application (Fig. S7).

3.6. Real sample analysis

In order to study the feasibility of MB/N-Mo_2C/GCE sensor in analyzing real samples, the content of m-NP in river water and tap water was determined. The water samples were first filtered with 0.22 μm polytetrafluoroethylene (PTFE) microporous filter membrane, and then mixed with PB (pH 7.0) at volumetric ratio of 1:4. Finally, m-

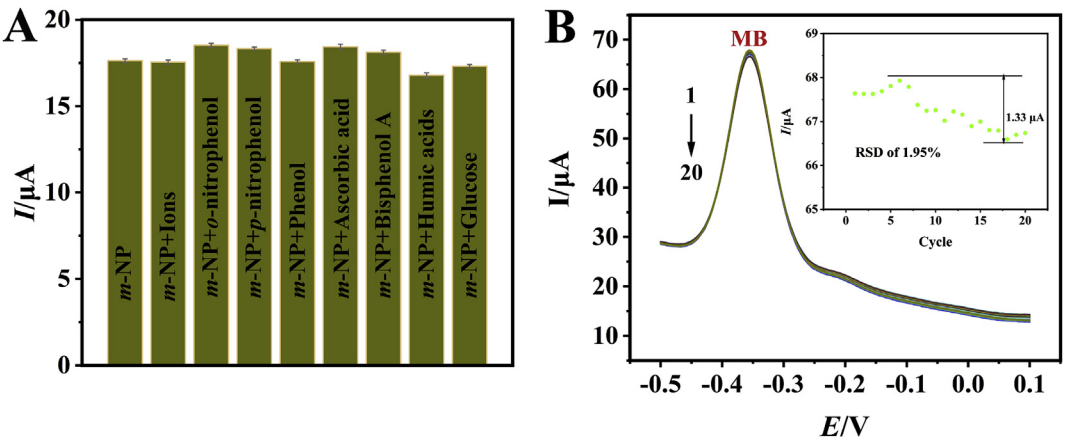

Fig. 5. (A) Sensing responses towards m-NP in the presence of decuple conentration of interfering substances using MB/N-Mo_2C/GCE. (B) SWV curves of MB/N-Mo_2C/GCE in 0.1 M PB continuous scan of 20 times. Inset of B is the peak currents of the SWV curves.

NP standard solution at different concentrations was added to the prepared water samples and detected using the as-obtained ratio sensor. The results listed in Table S2 show that the recoveries of m-NP were from 98.83% to 101.4%, indicating admirable accuracy of MB/N-Mo_2C/GCE in measuring m-NP in water samples. In addition, we verified the reliability of the sensor using UV–Visible spectrophotometer (Table S3). By comparing the results of the two experiments, it is found that there is no obvious difference, indicating that the newly established sensor platform is able to analyze actual samples.

4. Conclusions

In this study, for the first time, we assembled MB and N-Mo_2C to design a novel ratio electrochemical sensor. By detecting the model analyte, m-NP, the sensing performance of the newly developed composite ratiometric sensor was fully investigated. It was found that the sensor was sensitive and selective, together with a wide linear range toward m-NP. More importantly, by using the ratiometric signal to determine the concentration of m-NP, the sensing performance of was greatly enhanced, in the aspects of stability, repeatability and robustness. Real sample measurements further confirmed the very good practicability of the sensor. However, a natural disadvantage is the presence of electrode fouling in the system, and future work will focus on introduction of super hydrophobic material or appropriate anti-electrode passivation substance (such as polyoxometalates) for the purpose of diminishing fouling impact. It is worth noting that this strategy is flexible and versatile, therefore expectable to be used for constructing various ratio sensors to detect other analytes.

CRediT authorship contribution statement

Hailong Ren: Conceptualization, Methodology, Software, Data curation, Writing - original draft, Writing - review & editing. **Jingjing Wang:** Resources, Formal analysis. **Huanhuan Feng:** Data curation, Writing - review & editing. **Yingchun Li:** Project administration, Writing - review & editing, Supervision. **Bang-Ce Ye:** Project administration, Writing - review & editing.

Declaration of competing interest

The authors declare that they have no known competing financial interests or personal relationships that could have appeared to influence the work reported in this paper.

Acknowledgements

The project was financially supported by National Natural Science Foundation of China (21575089, 81773680) and Innovation and entrepreneurship project for overseas high-level talents of Shenzhen (KQJSCX20180328165437711).

Appendix A. Supplementary data

Supplementary data to this article can be found online at https://doi.org/10.1016/j.bios.2019.111663.

References

Asadpour-Zeynali, K., Najafi-Marandi, P., 2011. Electroanalysis 23 (9), 2241–2247.
Belloli, Barletta, Bolzacchini, Meinardi, Orlandi, Rindone, 1999. J. Chromatogr. A 846 (1–2), 277–281.
Berit, H., Poul Georg, M., Jacob, B., Rgensen, J., K.P., Nielsen, J.H., Sebastian, H., Ib, C., Rskov, N., J.K., 2005. J. Am. Chem. Soc. 127 (15), 5308–5309.
Chen, J., Yang, H., Xu, X., Su, Z., Guo, Y., Wang, Q., 2018. Appl. Surf. Sci. 455, 187–194.
Chen, Y.Y., Zhang, Y., Jiang, W.J., Zhang, X., Dai, Z., Wan, L.J., Hu, J.S., 2016. ACS Nano 10 (9), 8851.
Chu, L., Han, L., Zhang, X.L., 2011. J. Appl. Electrochem. 41 (6), 687–694.
Du, C., Huang, H., Wu, Y., Wu, S., Song, W., 2016. Nanoscale 8 (36), 16251–16258.
Feng, P.L., Hang, L.Y., Shuang, Y., Fei, L.P., Quan, Y.M., Gui, Y.H., 2014. Chem. Commun. 50 (86), 13135–13137.
Gu, Y.E., Zhang, Y., Zhang, F., Wei, J., Wang, C., Du, Y., Ye, W., 2011. Electrochim. Acta 56 (2), 953–958.
Guo, X., Wang, Z., Zhou, S., 2004. Talanta 64 (1), 135–139.
Hanjun, C., Xiaoyu, W., Hui, W., 2015. Anal. Chem. 87 (17), 8889–8895.
Honeychurch, K.C., Hart, J.P., 2010. Electroanalysis 19 (21), 2176–2184.
Jing, Z., Ma, J., Zhang, Y., Lei, H., Wan, Q., 2014. J. Chem. Technol. Biot. 89 (2), 259–264.
Kong, Q., Xi, W., Tang, A., Duan, W., Bo, L., 2016. Mater. Lett. 177, 139–142.
Li, X., Kan, X., 2018. Analyst 143 (9), 2150.
Li, Y., Liu, J., Zhang, Y., Gu, M., Wang, D., Dang, Y.Y., Ye, B.C., Li, Y., 2018. Biosens. Bioelectron. 106, 71–77.
Li, Y., Song, H., Zhang, L., Zuo, P., Ye, B.C., Yao, J., Chen, W., 2016. Biosens. Bioelectron. 78, 308.
Liu, J., Tang, S., Lu, Y., Cai, G., Chen, X., 2013. Energy Environ. Sci. 6 (9), 2691–2697.
Liu, L., Liu, L., Wang, Y., Ye, B.-C., 2019. Talanta 199, 478–484.
Liu, Z., Ma, X., Zhang, H., Lu, W., Ma, H., Hou, S., 2012. Electroanalysis 24 (5), 1178–1185.
Luo, L.Q., Zou, X.L., Ding, Y.P., Wu, Q.S., 2008. Sens. Actuators B Chem. 135 (1), 61–65.
Mcenaney, J.M., Crompton, J.C., Callejas, J.F., Popczun, E.J., Schaak, R.E., 2014. Chem. Mater. 26 (16), 4826–4831.
Niazi, A., Yazdanipour, A., 2007. J. Hazard Mater. 146 (1), 421–427.
Pearson, J., 1948. Trans. Faraday Soc. 44, 683–697.
Perry, D.A., Son, H.J., Cordova, J.S., Smith, L.G., Biris, A.S., 2010. J. Colloid Interface Sci. 342 (2), 311–319.
Pu, Z., Wang, M., Kou, Z., Amiinu, I.S., Mu, S., 2016. Chem. Commun. 52 (86), 12753.
Shi, Q., Diao, G., 2011. Electrochim. Acta 58 (1), 399–405.
Silvester, D.S., Wain, A.J., Aldous, L., Hardacre, C., Compton, R.G., 2006. J. Electroanal. Chem. 596 (2), 131–140.
Vondrák, J., 1983. Surf. Technol. 20 (1), 91–92.
Wang, C., Yuan, R., Chai, Y., Hu, F., 2012. Anal. Methods 4 (6), 1626–1628.

Wang, D., Huang, B., Liu, J., Guo, X., Abudukeyoumu, G., Zhang, Y., Ye, B.C., Li, Y., 2017. Biosens. Bioelectron. 102, 389.
Wang, H., Wang, Y., Liu, S., Yu, J., Guo, Y., Xu, Y., Huang, J., 2016. Biosens. Bioelectron. 80, 471–476.
Wei, T., Huang, X., Qiang, Z., Wang, L., 2015. J. Electroanal. Chem. 743, 105–111.
Xia, Z., Liang, W., Zhou, J., Zhang, X., Chen, J., 2015. J. Electroanal. Chem. 742, 97–103.
Xu, X., Liu, Z., Zhang, X., Duan, S., Xu, S., Zhou, C., 2011. Electrochim. Acta 58, 142–149.
Yan, D., Byung Joon, L., Bingling, L., Sherry, J.Y., Sessler, J.L., Ellington, A.D., 2014. Anal. Chem. 86 (15), 8010–8016.
Yao, C., Sun, H., Fu, H.F., Tan, Z.C., 2015. Electrochim. Acta 156 (Pt7), 163–170.
Yi, Z., Guang Ming, Z., Lin, T., Yuan, Z., Xiao Xiao, H., Yan, H., 2015. Anal. Chem. 87 (2), 989–996.
Yu, J., Jin, H., Gui, R., Wang, Z., Ge, F., 2017. Talanta 162 (Complete), 435–439.
Zhang, J., Cui, S., Ding, Y., Yang, X., Guo, K., Zhao, J.-T., 2018a. Biosens. Bioelectron. 112, 177–185.
Zhang, J., Wang, D., Li, Y., 2019. ACS Appl. Mater. Interfaces.
Zhang, R., Yang, Z., Deng, X., Sun, S., Li, Y., 2018b. Electrochim. Acta 271.
Zhang, W., Liu, L., Yangguang, L., Dongyang, W., Heng, M., Hailong, R., Yulin, S., Yajie, H., Bang-Ce, Y., 2018c. Biosens. Bioelectron. 121, 96–103.
Zhang, T., Lang, Q., Yang, D., Liang, L., Zeng, L., Cheng, Z., Li, T., Wei, M., Liu, A., 2013. Electrochim. Acta 106 (2013), 127–134.
Zhu, Y., Chen, G., Xu, X., Yang, G., Shao, Z., 2017. ACS Catal. 3540–3547.